

Nonlinear optical Hall effect in Weyl semimetal WTe₂

Young-Gwan Choi

Sungkyunkwan University

Manh-Ha Doan

Department of Energy Science, Sungkyunkwan University, Suwon 16419, Republic of Korea

Youngkuk Kim

Sungkyunkwan University <https://orcid.org/0000-0002-1680-7007>

Gyung-Min Choi (✉ gmchoi@skku.edu)

Sungkyunkwan University <https://orcid.org/0000-0002-2501-042X>

Article

Keywords: Non-magnetic Systems, Berry Curvature, Nonlinear Kerr Rotation, Fourth-order Nonlinearity, Anisotropy

Posted Date: March 1st, 2021

DOI: <https://doi.org/10.21203/rs.3.rs-228103/v1>

License:   This work is licensed under a Creative Commons Attribution 4.0 International License.

[Read Full License](#)

1 **Nonlinear optical Hall effect in Weyl semimetal WTe₂**

2
3 Young-Gwan Choi^{1†}, Manh-Ha Doan^{1†}, Youngkuk Kim^{2,3}, and Gyung-Min Choi^{1,3*}

4
5 ¹ Department of Energy Science, Sungkyunwan University, Suwon 16419, Korea

6 ² Department of Physics, Sungkyunwan University, Suwon 16419, Korea

7 ³ Center for Integrated Nanostructure Physics, Institute for Basic Science, Suwon 16419, Korea

8
9 †These authors contribute equally

10 *E-mail: gmchoi@skku.edu

11
12 **The ordinary Hall effect refers to generation of a transverse voltage upon exertion of an**
13 **electric field in the presence of an out-of-plane magnetic field. While a linear Hall effect**
14 **is commonly observed in systems with breaking time-reversal symmetry *via* an applied**
15 **external magnetic field or their intrinsic magnetization^{1, 2}, a nonlinear Hall effect can**
16 **generically occur in non-magnetic systems associated with a nonvanishing Berry**
17 **curvature dipole³. Here we report, observations of a nonlinear optical Hall effect in a**
18 **Weyl semimetal WTe₂ without an applied magnetic field at room temperature. We**
19 **observe an optical Hall effect resulting in a polarization rotation of the reflected light,**
20 **referred to as the nonlinear Kerr rotation. The nonlinear Kerr rotation linearly depends**
21 **on the charge current and optical power, which manifests the fourth-order nonlinearity.**
22 **We quantitatively determine the fourth-order susceptibility, which exhibits strong**
23 **anisotropy depending on the directions of the charge current and the light polarization.**
24 **Employing symmetry analysis of Berry curvature multipoles, we demonstrate that the**

25 **nonlinear Kerr rotations can arise from the Berry curvature hexapole allowed by the**
26 **crystalline symmetries of WTe₂. There also exist marginal signals that are incompatible**
27 **with the symmetries, which suggest a hidden phase associated with the nonlinear process.**

28 Whereas the ordinary Hall effect of electrons discovered in 1879 by Edwin H. Hall commonly
29 arises in a two-dimensional conductor under a perpendicular magnetic field, the Hall effect has
30 become a ubiquitous phenomenon, occurring in various systems ranging from magnetic
31 insulators to non-magnetic semiconductors^{1,2}. Notably, the nonlinear Hall effect has been
32 theoretically predicted and experimentally observed in a *non-magnetic* system under a time-
33 reversal symmetric condition³⁻⁶. This finding stands a contrast to the *a priori* sense that the Hall
34 effect should occur without time-reversal symmetry, since time-reversal symmetry zeroes the
35 Chern number, which dictates the quantized Hall conductance of the two-dimensional
36 electrons^{7,8}. The key innovation was to reveal that it is only in the first-order response regime
37 that time-reversal symmetry suppresses the Hall voltage, in which the Hall voltage is linearly
38 proportional to a driving electric field (*E*-field), and the Hall conductivity is independent of *E*-
39 field. In the case of a higher-order response regime, the presence of time-reversal symmetry
40 rather allows for a new opportunity to encounter a novel Hall effect, namely a nonlinear Hall
41 effect^{3,9-11}. Time-reversal symmetry in the absence of inversion symmetry enables a dipolar
42 distribution of the Berry curvature, which leads to the nonzero integration of the Berry
43 curvature gradient in momentum space, dubbed the Berry curvature dipole^{3,4}. Consequently,
44 a second-order nonlinear Hall voltage dominates the Hall effect, induced by the Berry curvature
45 dipole, and the Hall voltage (conductivity) features a quadratic (linear) dependence on *E*-field.
46 Theoretically, it is possible that crystalline symmetries can further suppress the second-order
47 nonlinear Hall effect with the help of time-reversal symmetry. Therefore, a higher-order
48 nonlinear Hall effect can emerge¹²⁻¹⁴, which is yet to be addressed experimentally.

49 The Hall effect is responsible for not only electrical responses but also optical responses
50 of electrons, which is referred to as the optical Hall effect¹⁵. The linear optical Hall response is
51 widely used to measure magnetization of a system *via* magneto-optic Faraday effect, magneto-
52 optic Kerr effect, or magnetic circular dichroism¹⁶. When light passes through (Faraday rotation)

53 or is reflected from (Kerr rotation) magnetized mediums, its polarization rotates. In this case,
54 the rotation angle, which is linearly proportional to the Hall conductivity σ_{xy} , is independent
55 on E -field of light, but depends on the light's frequency (ω). This polarization rotation arises
56 owing to the optical Hall effect, in which an E -field of an incident light induces a transverse E -
57 field. The optical detection of the nonlinear electrical Hall effect is also reported in a strained
58 MoS₂ monolayer, where the Hall conductivity is driven by an external charge current and
59 independent on E -field of light¹⁷.

60 The optical Hall effect is an ideal platform to investigate high-order nonlinear processes
61 owing to the intense E -field of a short-pulsed laser. A strong nonlinear optical effect has been
62 often discovered with topologically non-trivial materials, associated with topological quantities,
63 such as the Berry curvature, responsible for various nonlinear optical effects, including shift
64 current, second-harmonic generation, and nonlinear Kerr rotation¹². A two-dimensional
65 massless Dirac system, such as graphene, has been extensively studied for exceptionally large
66 nonlinear optical activities from terahertz to near infrared regime¹⁸⁻²⁰. Recently, enhanced large
67 nonlinear optical responses have been observed in three-dimensional topological Dirac/Weyl
68 semimetals, e.g. photocurrent²¹⁻²³, second- or third-harmonic generation^{12, 24}, and optical Kerr
69 effect^{25, 26}. Furthermore, an anomalously large coefficient for the linear magneto-optic Kerr
70 effect has been reported with a magnetic Weyl semimetal²⁷. Tungsten ditelluride, WTe₂, known
71 as type-II Weyl semimetal²⁸⁻³⁰, can be a good platform to investigate the nonlinear optical
72 response. Previously, the topological properties of WTe₂ have been studied mainly by electrical
73 transport measurements, such as negative magnetoresistance, planar Hall effect, and electrical
74 Hall effect^{29, 31-34}.

75 In this work, we demonstrate, for the first time, the current-induced nonlinear optical Hall
76 effect in multilayer WTe₂ Weyl semimetal, which measures the analogue of the fourth-order

77 nonlinear Hall effect under a time-reversal symmetric condition. The polarization rotation is
78 measured at room temperature without application of magnetic field. In analogy with the
79 magneto-optical Kerr rotation, which corresponds to a linear optical Hall effect, we call our
80 observation as the nonlinear Kerr rotation. Our Kerr rotation should be distinguished from the
81 well-known optical Kerr effect, which is 3rd order nonlinear effect but is not the Hall effect.
82 The optical Kerr effect is driven by the diagonal part of the dielectric tensor, and its mechanism
83 is related to the anharmonic potential of bound electrons. Whereas, our Kerr rotation is driven
84 by the off-diagonal part of the dielectric tensor, and its mechanism is related to the Berry
85 curvature (shown later). We give a precise fingerprint of the fourth-order nonlinearity by
86 showing that the Kerr angle is proportional to the cube of the electric field: linear in the
87 displacement field of charge current and quadratic in the driving field of the light. Our findings
88 suggest that WTe₂ can be used for the electrically controllable nonlinear-optic-medium. The
89 corresponding fifth-rank susceptibility tensor is quantitatively determined with different
90 directions of the charge current and light polarization, leading to the maximum susceptibility
91 of $\sim 10^{-24} \text{ m}^3 \text{ V}^{-3}$. The fourth-order nonlinearity suggests the mechanism based on a non-
92 vanishing Berry curvature hexapole. This predicts the dominant components of the
93 susceptibility comprise those compatible with the crystalline symmetries of WTe₂, which is in
94 line with the observations. Residual signals exist from symmetry-incompatible components,
95 which can be an indicative of a possible hidden phase during the nonlinear process.

96 Our experiment is based on multilayer WTe₂ with thickness of 50~70 nm, exfoliated on
97 SiO₂/Si substrates from WTe₂ bulk crystal (see Methods). Figure 1a shows a top view of its
98 crystal structure. The crystal orientations (*a*- and *b*-axis directions) of the exfoliated flakes are
99 precisely determined by polar Raman spectroscopy (Fig. 1b and Supplementary Information
100 S1)^{35, 36} and transmission electron microscope techniques (Fig. 1c and Supplementary

101 Information S2). The electrical electrodes are fabricated along the a - and b -axes of WTe₂ by
102 electron-beam lithography following by a deposition of Cr/Au metals (Fig. 1d). Our fabricated
103 devices show metallic behavior of WTe₂ with linear current-voltage characteristics (Fig. 1e)
104 and the known temperature dependences of resistance (Fig. 1f). The resistance anisotropy ratio
105 between the b - and a -axis directions is about 1.5, which is also in good agreement with the
106 literature value^{5, 37} (Supplementary Information S3).

107 For studying electro-optical phenomena in WTe₂ devices, we adopt the polarization
108 rotation microscopy in a reflection geometry with an application of oscillating charge current
109 \vec{j}_c (Fig. 2a). A pulsed laser with a linear polarization, the center wavelength 785 nm ($\omega \sim$
110 $1.6 \text{ eV}/\hbar$), and the pulse duration ~ 100 fs is applied to the devices. After reflection from the
111 devices, polarization variation, e.g. rotation and ellipticity angles, is monitored (see Methods).
112 Current-induced Kerr rotation can be expressed as $\Delta\tilde{\theta}_K^\omega(\vec{j}_c) \equiv \tilde{\theta}_K^\omega(\vec{j}_c) - \tilde{\theta}_K^\omega(0)$, where
113 $\tilde{\theta}_K^\omega(\vec{j}_e)$ and $\tilde{\theta}_K^\omega(0)$ are complex Kerr angles in the optical first-harmonic mode with and
114 without the charge current, respectively (details in Supplementary Information S4). The \vec{j}_c is
115 converted to the displacement field \vec{D} employing $\vec{D} = \rho\vec{j}_c$, where ρ is the resistivity of
116 WTe₂. (Note that \vec{D} and \vec{E} are used to differentiate the fields of the charge current and the
117 incident light, respectively.)

118 We first demonstrate the fourth-order nonlinearity of the observed Kerr rotation. Figure
119 2b shows that the Kerr rotation is a linear function of D_b , which is the b -component of the
120 displacement vector \vec{D} . Moreover, when the direction of the D_b is reversed, the sign of Kerr
121 angle direction is also changed, implying that the chirality of the system can be electrically
122 switched. We note that the current-induced Kerr rotation only occurs with a pulsed laser but
123 not with a continuous-wave laser of the same time-average power. This result suggests that the
124 Kerr rotation is nonlinear in terms of the electric field of light \vec{E} . At the same time-average

125 power, a femtosecond pulsed laser carries a much higher intensity of \vec{E} compared to that of
 126 the continuous wave laser. Indeed, the Kerr rotation shows a linear dependence on the optical
 127 power of a pulsed laser. (The Kerr rotation is measured from a photocurrent of a balanced
 128 detector as $\Delta\tilde{\theta}_K^\omega(j_e) = \frac{\Delta I}{2I_0}$, where I_0 is the total photocurrent by reflected light and ΔI is the
 129 change of the photocurrent by the polarization rotation of light. The raw data of ΔI show a
 130 quadratic dependence on the optical power.) The linear dependence on the optical power
 131 indicates that $\Delta\tilde{\theta}_K^\omega(j_e) \propto E_i E_j$ as $I = nc\varepsilon_0 |\vec{E}|^2$, where n is the refractive index, c is the
 132 speed of light, ε_0 is the vacuum permittivity. This result is in stark contrast to the linear optical
 133 Hall effect, dubbed magneto-optical Kerr rotation, in which the Kerr rotation is independent
 134 on \vec{E} . Based on these results, we conclude that the Kerr rotation of WTe₂ has a cube
 135 dependence on the fields $\Delta\tilde{\theta}_K^\omega(j_e) \sim D_b |\vec{E}|^2$, and thus demonstrates the fourth-order
 136 nonlinearity of the Hall effect.

137 Having established the fourth-order nonlinearity, we explore the anisotropic nature of the
 138 observed Kerr rotation. We perform a two-dimensional scanning of the Kerr rotation with
 139 different polarization directions of a linearly polarized light and displacement field as shown
 140 in Fig. 3. The Kerr rotation appears prominently throughout the sample area when the
 141 displacement field $\vec{D} \parallel \hat{b}$ and light field $\vec{E} \parallel \hat{a}$ (Fig. 3b). When both \vec{D} and \vec{E} are aligned
 142 along the b -axis ($\vec{D} \parallel \hat{b}$ and $\vec{E} \parallel \hat{b}$), there still exists finite uniform signal, but the intensity is
 143 significantly weakened compared to the first case (Fig. 3c). More importantly, when $\vec{D} \parallel \hat{a}$, it
 144 results in negligible signals, irrespective of the polarization direction as shown in Fig. 3e and
 145 Fig. 3f. Consequently, the Kerr rotation occurs prominently when $\tilde{\theta}_K^\omega(j_e) \sim D_b E_a^2$ and
 146 marginally when $\tilde{\theta}_K^\omega(j_e) \sim D_b E_b^2$. These features are stark contrast to the second-order
 147 nonlinear Hall effect, in which the displacement field in $\vec{D} \parallel \hat{a}$ gives a rise to the electric Hall

148 voltage.^{4,5}

149 We, then, quantitatively analyze the nonlinear Kerr rotation and make connection with the
150 fourth-order nonlinear Hall conductivity. Under the action of the electric field $\vec{E}(\omega)$ of the
151 light incident along the sample \hat{c} -direction, the Kerr rotation with an initial polarization along
152 a - and b -directions can be expressed as,

$$153 \quad \Delta\tilde{\theta}_K^{ba} \approx \frac{-2\varepsilon_{ba}}{(n_a + n_b)(1 - n_a)(1 + n_n)}, \quad (1)$$

$$154 \quad \Delta\tilde{\theta}_K^{ab} \approx \frac{2\varepsilon_{ab}}{(n_a + n_b)(1 + n_a)(1 - n_b)}, \quad (2)$$

155 where $\varepsilon_{\mu\delta}$ ($\mu \neq \delta$), with subscript denotes the crystal axis, is the off-diagonal components of
156 the dielectric tensor, which is related with the Hall conductivity as $\varepsilon_{\mu\delta} = \frac{1}{i\varepsilon_0\omega}\sigma_{\mu\delta}$, and n_μ is
157 the refractive index with the light polarization along the μ -direction (see Supplementary
158 Information S5 for the derivation.). Since the Kerr rotation comes from the fourth-order
159 nonlinear process, we can express the $\varepsilon_{\mu\delta}$ in terms of a fourth-order susceptibility tensor
160 $\chi_{\mu\alpha\beta\gamma\delta}^{(4)}$ as

$$161 \quad \varepsilon_{\mu\delta} = \chi_{\mu\alpha\beta\gamma\delta}^{(4)} D_\alpha(0) E_\beta(\omega) E_\gamma^*(-\omega). \quad (3)$$

162 As an example, when \vec{D} is applied along the sample b -axis, and \vec{E} is along the a -axis (Fig.
163 3b), $\varepsilon_{ba} = \tilde{\chi}_{bbaaaa}^{(4)} D_b E_a(\omega) E_a^*(-\omega)$ is responsible for the Kerr rotation. On the other hand,
164 when all fields are aligned along the b -axis (Fig. 3c), the Kerr rotation arises from $\varepsilon_{ab} =$
165 $\tilde{\chi}_{abbbbb}^{(4)} D_b E_b(\omega) E_b^*(-\omega)$. Comparing the measured Kerr rotation (real and imaginary parts)
166 with equations (1) and (2), we obtain $\tilde{\chi}_{bbaaaa}^{(4)} = (6.2 - i1.6) \times 10^{-25} \text{ m}^3 \text{ V}^{-3}$ and $\tilde{\chi}_{abbbbb}^{(4)} =$
167 $(-2.5 - i2.5) \times 10^{-25} \text{ m}^3 \text{ V}^{-3}$. We also measure the Kerr rotation with arbitrary direction of

168 E of light by changing the polarization direction in three-dimensional way: the azimuthal angle
169 θ in the ab plane; the polar angle ψ in the ab plane; the polar angle φ in the bc plane
170 (Fig. 4). From the θ dependence of the Kerr rotation, we confirm the additional contribution
171 from $\tilde{\chi}_{ababb}^{(4)}$ and $\tilde{\chi}_{bbbbba}^{(4)}$. (To fit the experimental data, we use the Jones matrix formalism.
172 See Supplementary Information S6). In addition, from the polar angle dependence, we identify
173 contributions of $\tilde{\chi}_{bbaac}^{(4)}$ and $\tilde{\chi}_{abbbc}^{(4)}$ to the Kerr rotation. In particular, the magnitude of
174 $\tilde{\chi}_{bbaac}^{(4)}$ of $> 2.7 \times 10^{-24} \text{ m}^3 \text{ V}^{-3}$ is much larger than those of $\tilde{\chi}_{abbbb}^{(4)}$ and $\tilde{\chi}_{abbbb}^{(4)}$. As the
175 fourth-order susceptibility is unexplored in other materials, to our best knowledge, it can be
176 informative to convert the fourth-order susceptibility to the third-order susceptibility as
177 $\tilde{\chi}_{baac}^{(3)} = \tilde{\chi}_{bbaac}^{(4)} D_b$. With D_b of $6 \times 10^3 \text{ V m}^{-1}$, we obtain $\tilde{\chi}_{baac}^{(3)}$ of $> 1.6 \times$
178 $10^{-20} \text{ m}^2 \text{ V}^{-2}$, which is even larger than typical optical nonlinear systems, such as nanoparticle
179 or polymer structures^{38, 39}. Therefore, our result demonstrates a new functionality, electrical
180 control of the optical nonlinear process, with topological materials.

181 Now, we provide a symmetry argument that explains the dominance of fourth-order
182 nonlinear susceptibility $\chi_{\mu\alpha\beta\gamma\delta}^{(4)}$ for the Kerr rotation of WTe₂. Using the Boltzmann equation
183 approaches, previous studies have shown that the fourth-order nonlinear susceptibility $\chi_{\mu\alpha\beta\gamma\delta}^{(4)}$
184 can be expressed as^{13, 14},

$$185 \quad \chi_{\mu\alpha\beta\gamma\delta}^{(4)}(\omega) = \frac{e^5}{i\varepsilon_0\omega\hbar^4} \int \frac{d^3\mathbf{k}}{(2\pi)^3} f_{\text{FD}} \left(-i \frac{\partial_\alpha \partial_\beta \partial_\gamma \partial_\delta v_\mu}{3\tilde{\omega} 2\tilde{\omega} \tilde{\omega}^2} - \frac{\partial_\alpha \partial_\beta \partial_\gamma \Omega_{\mu\delta}}{2\tilde{\omega} \tilde{\omega}^2} \right), \quad (4)$$

186 where e is the elementary charge, \hbar is the reduced Planck constant, f_{FD} is the Fermi-Dirac
187 distribution, $\partial_\alpha \equiv \frac{\partial}{\partial k_\alpha}$, $\tilde{n}\tilde{\omega} = n\omega + i/\tau$, n is integer, ω is the angular frequency of light, τ is
188 the relaxation time, and $\Omega_{\alpha\beta}$ is the Berry curvature with a pseudovector form of $B_\gamma =$
189 $\frac{1}{2} \varepsilon_{\alpha\beta\gamma} \Omega_{\alpha\beta}$. The integration is done over the first Brillouin zone. The first term in the integrand

190 is the Drude-like term, and the second term is related with the Berry curvature hexapole
 191 moment (see Supplementary Information S7 for the derivation). The existence of $\chi_{\mu\alpha\beta\gamma\delta}^{(4)}$ can
 192 be argued based on the symmetry consideration. The T_d -phase of WTe_2 belongs to an
 193 orthorhombic space group of $Pmn2_1$ and point group of $2mm$. It has a mirror reflection in the
 194 bc -plane (M_a) and a glide mirror reflection in ac -plane (M_b). It also preserves a time-reversal
 195 symmetry (\mathcal{T}) without an applied magnetic field, and the Drude-like term vanishes under the
 196 \mathcal{T} symmetry. The Berry curvature hexapole gives four non-zero terms at the presence of the
 197 M_a , M_b , and \mathcal{T} symmetry: $\partial_a\partial_a\partial_a\Omega_{ca}$, $\partial_a\partial_b\partial_b\Omega_{ca}$, $\partial_a\partial_a\partial_b\Omega_{cb}$, and $\partial_b\partial_b\partial_b\Omega_{cb}$.
 198 Specifically, the M_a and M_b symmetries force $\partial_\alpha\partial_\beta\partial_\gamma\Omega_{\mu\delta}$ to vanish when it contains an odd
 199 number of momentum index of a or b . Since we measure the in-plane rotation ($\Delta\theta_K^{ba}$ or $\Delta\theta_K^{ab}$),
 200 only $\partial_a\partial_b\partial_b\Omega_{ca}$ and $\partial_a\partial_a\partial_b\Omega_{cb}$ terms are relevant. Then, the corresponding symmetry-
 201 allowed susceptibilities are $\tilde{\chi}_{abbca}^{(4)}$ and $\tilde{\chi}_{aabcb}^{(4)}$. If we allow the permutation among the
 202 subscript indexes, this prediction corresponds to $\tilde{\chi}_{bbaac}^{(4)}$, which is the largest susceptibility of
 203 our measurement. However, the symmetry consideration cannot explain other residual
 204 measurements, such as $\tilde{\chi}_{bbaaa}^{(4)}$ and $\tilde{\chi}_{abbbb}^{(4)}$. Note that even without the M_b symmetry,
 205 which can be broken in a few layers of WTe_2 by the surface effect, $\tilde{\chi}_{bbaaa}^{(4)}$ and $\tilde{\chi}_{abbbb}^{(4)}$ should
 206 be vanished by the M_a symmetry. As a possible explanation, we expect that a strong E -field of
 207 light might influence the crystal structure such that it spontaneously lowers the crystalline
 208 symmetry of WTe_2 . For example, a back-gate bias was employed to induce the inversion
 209 symmetry breaking, which controls the Berry curvature dipole, in a monolayer and bilayer
 210 WTe_2 ^{6, 23}. In addition, it has been reported that a terahertz light pulse can induce an ultrafast
 211 switch in symmetry of WTe_2 via lattice strain⁴⁰. Furthermore, the semiclassical picture can
 212 potentially miss the possible quantum effects, notably associated with the multiband nature of
 213 WTe_2 at a sizable angular frequency $\hbar\omega = 1.6$ eV, as discussed by Parker *et. al* (ref. 14). A

214 detailed mechanism for the light-induced symmetry change would be an interesting topic for
215 further study.

216 For a mechanism other than the Berry curvature multipoles, the chirality of the Weyl point
217 in Weyl semimetals can directly induce nonlinear optical processes, such as photocurrent or
218 circular photogalvanic effect²¹⁻²³. Interestingly, ref. ²³ reported a photocurrent response that is
219 forbidden by the symmetry of a material of TaIrTe₄. Authors of ref. ²³ interpreted the symmetry-
220 forbidden response as a result of combination of the built-in electric field and optical excitation.
221 Nonetheless, the chiral selection occurs with an optical transition from the lower part of the
222 Weyl cone to the upper part, so it is mainly observed low photon energy. For connecting this
223 effect to our work, further study is needed.

224 In summary, we observe the current-induced nonlinear optical Hall effect in WTe₂
225 multilayers at room temperature. The optical Hall effect is revealed as the nonlinear Kerr
226 rotation, and the fourth-order nonlinearity is confirmed by the linear dependence on the charge
227 current and optical power. Our work shows that the nonlinear optical process can be controlled
228 by a small electric bias, thereby, demonstrates a useful functionality for the electro-optic device
229 employing topological materials. From the anisotropic behavior of the Hall response, we
230 quantitatively determine various the fourth-order susceptibilities ($\chi_{\mu\alpha\beta\gamma\delta}^{(4)}$). For the mechanism
231 of $\chi_{\mu\alpha\beta\gamma\delta}^{(4)}$, we considered the Berry curvature hexapole, and it can explain the existence of
232 $\tilde{\chi}_{bbaac}^{(4)}$, the largest susceptibility of our measurements. However, we found that some of our
233 measurements, such as $\tilde{\chi}_{bbaaa}^{(4)}$ and $\tilde{\chi}_{abbbb}^{(4)}$, were forbidden by the symmetry of WTe₂. The
234 observation of the symmetry forbidden terms suggests that not only a stable phase but also
235 other unknown phases participate during the nonlinear process. We expect that the fourth-order
236 nonlinear optical Hall effect could be a useful tool to investigate the topological nature of Weyl
237 semimetal.

238

239 **Methods**

240 *Device Fabrication:* WTe₂ multilayer flakes are exfoliated from the WTe₂ bulk crystal
241 onto SiO₂/Si substrates by using the scotch tape method inside a glove box with an argon
242 environment to prevent oxidation. The sample is then coated by a PMMA layer before being
243 taken out for Raman investigation and device fabrication. The in-plane crystal orientation (*a*-
244 and *b*-axis) of the WTe₂ flake is determined by using an angle dependent polarized Raman
245 spectroscopy (Supplementary Information S1). Cr/Au metal electrodes are fabricated along
246 these two axes by the e-beam lithography and e-beam evaporation processes, respectively. The
247 device is then etched by a reactive ion etching (RIE) system using SF₆ gas at high vacuum to
248 form a well-defined shape and is immediately loaded into the vacuum chamber of a RF
249 sputtering system for coating a thin SiN passivation layer to prevent surface degradation of
250 WTe₂ during the electrical and optical measurements. The thickness of the investigated devices
251 is from 50 to 70 nm, which is confirmed by the atomic force microscopy (AFM). After all
252 electrical and optical investigations, the crystal orientation of the fabricated devices is
253 reconfirmed by the transmission electron microscopy (TEM) measurements (Supplementary
254 Information S2).

255 *Electrical transport measurement:* The electrical characteristics of the fabricated device
256 are initially analyzed at room temperature under a high vacuum ($\sim 10^{-6}$ Torr) in a probe station
257 system with a Keithley-4200SCS parameter analyzer. The device is then bonded to a puck and
258 measured in a physical property measurement system (PPMS, Quantum Design) to investigate
259 the temperature-dependent transports. The resistance of the sample could be measured at
260 different temperatures which could be controlled at static or continuous scanning values in the
261 ranges of 2-300 K (Supplementary Information S3).

262 *Current-induced Kerr rotation microscopy:* A linearly polarized pulsed laser with the

263 center wavelength of 785 nm and a pulse duration ~ 100 fs is used as the excitation source.
264 After reflection of the linearly polarized light from the sample, the polarization variation, e.g.
265 the rotation and the ellipticity angles, can be monitored. For the normal incidence geometry,
266 the light polarization angle θ is defined with respect to the a -axis. The reflected laser beam
267 from the sample is passing through a half-wave plate, Wollaston prism, and the balanced
268 detector for monitoring polarization variation with/without quarter-wave plate before it.
269 Polarization variation can be precisely detected with a high sensitivity by using alternative bias
270 induced modulation and a lock-in amplifier for increasing signal-to-noise ratio. The bias-
271 induced Kerr angle can be expressed as, $\Delta\tilde{\theta}_K = \tilde{\theta}_K(j_c) - \tilde{\theta}_K(0)$, where $\tilde{\theta}_K$ is the complex
272 Kerr angle, j_c is the electrical current density, and $\Delta\tilde{\theta}_K$ is the variation of complex Kerr angle
273 with an application of electrical bias (for details, see Supplementary Information S4).
274

275 **Acknowledgements**

276 G.-M. C. acknowledges the National Research Foundation of Korea (NRF) grant funded
277 by the Korea government (2019R1C1C1009199, 2018M3D1A1058793). M.-H. D.
278 acknowledges the NRF (2019R1I1A1A01063236). Y. K. acknowledges the NRF
279 (2020R1A4A307970711). This study was supported by the Institute for Basic Science of Korea
280 (IBS-R011-D1). All authors thank to Jungcheol Kim and Hyeonsik Cheong in Sogang
281 university for their help with polarized Raman spectroscopy.

282

283 **Author contributions**

284 G.-M. C supervises the project. Y.-G. C and M.-H. D design the experiment, conduct
285 device fabrication and characterization, and data analysis. Y. K. provides a theoretical
286 consideration of the Berry curvature multipoles. All authors discuss the results and write the
287 manuscript.

288

289 **Competing interests**

290 The authors declare no competing interests

291

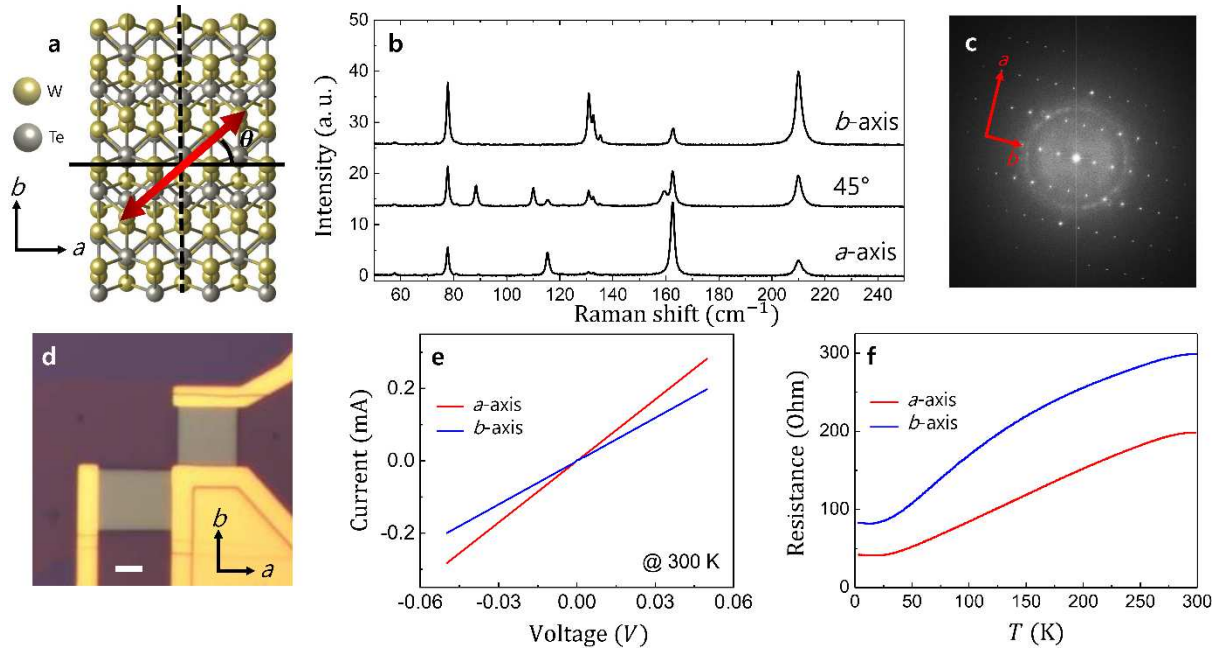
292 **Reference**

- 293 1. Nagaosa, N., Sinova, J., Onoda, S., MacDonald, A. H. & Ong, N. P. Anomalous Hall effect. *Reviews of*
294 *Modern Physics* **82**, 1539-1592 (2010).
- 295 2. von Klitzing, K. *et al.* 40 years of the quantum Hall effect. *Nat. Rev. Phys.* **2**, 397-401 (2020).
- 296 3. Sodemann, I. & Fu, L. Quantum Nonlinear Hall Effect Induced by Berry Curvature Dipole in Time-
297 Reversal Invariant Materials. *Phys. Rev. Lett.* **115**, 216806 (2015).
- 298 4. Ma, Q. *et al.* Observation of the nonlinear Hall effect under time-reversal-symmetric conditions. *Nature*
299
300
301

- 302 **565**, 337-342 (2019).
- 303
- 304 5. Kang, K., Li, T., Sohn, E., Shan, J. & Mak, K. F. Nonlinear anomalous Hall effect in few-layer WTe₂.
305 *Nat. Mater.* **18**, 324-328 (2019).
- 306
- 307 6. Xu, S.-Y. *et al.* Electrically switchable Berry curvature dipole in the monolayer topological insulator
308 WTe₂. *Nat. Phys.* **14**, 900-906 (2018).
- 309
- 310 7. Thouless, D. J., Kohmoto, M., Nightingale, M. P. & den Nijs, M. Quantized Hall Conductance in a Two-
311 Dimensional Periodic Potential. *Phys. Rev. Lett.* **49**, 405-408 (1982).
- 312
- 313 8. Prange, R. E. & Girvin, S. M. *The Quantum Hall Effect* (Springer, New York, 1987).
- 314
- 315 9. Low, T., Jiang, Y. J. & Guinea, F. Topological currents in black phosphorus with broken inversion
316 symmetry. *Phys. Rev. B* **92**, 235447 (2015).
- 317
- 318 10. Zhang, Y., van den Brink, J., Felser, C. & Yan, B. Electrically tuneable nonlinear anomalous Hall effect
319 in two-dimensional transition-metal dichalcogenides WTe₂ and MoTe₂. *2D Mater.* **5**, 0444001 (2018).
- 320
- 321 11. Du, Z. Z., Wang, C. M., Lu, H. Z. & Xie, X. C. Band Signatures for Strong Nonlinear Hall Effect in
322 Bilayer WTe₂. *Phys. Rev. Lett.* **121**, 266601 (2018).
- 323
- 324 12. Morimoto, T. & Nagaosa, N. Topological nature of nonlinear optical effects in solids. *Sci. Adv.* **2**,
325 e1501524 (2016).
- 326
- 327 13. Zhang, C.-P., Gao, X.-J., Xie, X.-J., Po, H. C. & Law, K. T. Higher-Order Nonlinear Anomalous Hall
328 Effects Induced by Berry Curvature Multipoles. Preprint at <https://arxiv.org/abs/2012.15628> (2021).
- 329
- 330 14. Parker, D. E., Morimoto, T., Orenstein, J. & Moore, J. E. Diagrammatic approach to nonlinear optical
331 response with application to Weyl semimetals. *Phys. Rev. B* **99**, 045121 (2019).
- 332
- 333 15. Schubert, M., Kuhne, P., Darakchieva, V. & Hofmann T. Optical Hall effect-model description: tutorial.
334 *J Opt Soc Am A Opt Image Sci Vis* **33**, 1553-1568 (2016).
- 335
- 336 16. Ebert, H. Magneto-optical effects in transition metal systems. *Rep. Prog. Phys.* **59**, 1665-1735 (1996).
- 337
- 338 17. Lee, J., Wang, Z., Xie, H., Mak, K. F. & Shan, J. Valley magnetoelectricity in single-layer MoS₂. *Nat.*
339 *Mater.* **16**, 887-891 (2017).
- 340
- 341 18. Yamashita, S. Nonlinear optics in carbon nanotube, graphene, and related 2D materials. *APL Photonics*
342 **4**, 034301 (2019).
- 343
- 344 19. Hendry, E., Hale, P. J., Moger, J., Savchenko, A. K. & Mikhailov, S. A. Coherent nonlinear optical
345 response of graphene. *Phys. Rev. Lett.* **105**, 097401 (2010).
- 346
- 347 20. Wang, J., Hernandez, Y., Lotya, M., Coleman, J. N. & Blau, W. J. Broadband Nonlinear Optical Response
348 of Graphene Dispersions. *Adv. Mater.* **21**, 2430-2435 (2009).

- 349
350 21. Chan, C.-K., Lindner, N. H., Refael, G. & Lee, P. A. Photocurrents in Weyl semimetals. *Phys. Rev. B* **95**,
351 041104(R) (2017).
- 352
353 22. Ma, Q. *et al.* Direct optical detection of Weyl fermion chirality in a topological semimetal. *Nat. Phys.* **13**,
354 842-847 (2017).
- 355
356 23. Ma, J. *et al.* Nonlinear photoresponse of type-II Weyl semimetals. *Nat. Mater.* **18**, 476-481 (2019).
- 357
358 24. Wu, L. *et al.* Giant anisotropic nonlinear optical response in transition metal monopnictide Weyl
359 semimetals. *Nat. Phys.* **13**, 350-355 (2016).
- 360
361 25. Zhang, T., Ooi, K. J. A., Chen W, Ang, L. K. & Ang, Y. S. Optical Kerr effect and third harmonic
362 generation in topological Dirac/Weyl semimetal. *Opt. Express* **27**, 38270-38280 (2019).
- 363
364 26. Zhong, Y., Feng, W., Liu, Z., Zhang, C. & Cao, J. C. Nonlinear optical conductivity of Weyl semimetals
365 in the terahertz regime. *Physica B: Conden. Matter* **555**, 81-84 (2019).
- 366
367 27. Higo, T, *et al.* Large magneto-optical Kerr effect and imaging of magnetic octupole domains in an
368 antiferromagnetic metal. *Nat. Photon.* **12**, 73-78 (2018).
- 369
370 28. Soluyanov, A. A. *et al.* Type-II Weyl semimetals. *Nature* **527**, 495-498 (2015).
- 371
372 29. Li, P. *et al.* Evidence for topological type-II Weyl semimetal WTe₂. *Nat. Commun.* **8**, 2150 (2017).
- 373
374 30. Lv, Y.-Y. *et al.* Experimental Observation of Anisotropic Adler-Bell-Jackiw Anomaly in Type-II Weyl
375 Semimetal WTe_{1.98} Crystals at the Quasiclassical Regime. *Phys. Rev. Lett.* **118**, 096603 (2017).
- 376
377 31. Ali, M. N. *et al.* Large, non-saturating magnetoresistance in WTe₂. *Nature* **514**, 205-208 (2014).
- 378
379 32. Li, P. *et al.* Anisotropic planar Hall effect in the type-II topological Weyl semimetal WTe₂. *Phys. Rev. B*
380 **100**, 205128 (2019).
- 381
382 33. Wang, Y. J., *et al.* Gate-tunable negative longitudinal magnetoresistance in the predicted type-II Weyl
383 semimetal WTe₂. *Nat. Commun.* **7**, 13142 (2016)
- 384
385 34. Zhang, C. *et al.* Room-temperature chiral charge pumping in Dirac semimetals. *Nat. Commun.* **8**, 13741
386 (2017).
- 387
388 35. Song, Q. *et al.* The in-plane anisotropy of WTe₂ investigated by angle-dependent and polarized Raman
389 spectroscopy. *Sci. Rep.* **6**, 29254 (2016).
- 390
391 36. Kim, M. *et al.* Determination of the thickness and orientation of few-layer tungsten ditelluride using
392 polarized Raman spectroscopy. *2D Mater.* **3**, 034004 (2016).
- 393
394 37. Choi, Y. B. *et al.* Evidence of higher-order topology in multilayer WTe₂ from Josephson coupling through
395 anisotropic hinge states. *Nat. Mater.* **19**, 974-979 (2020).

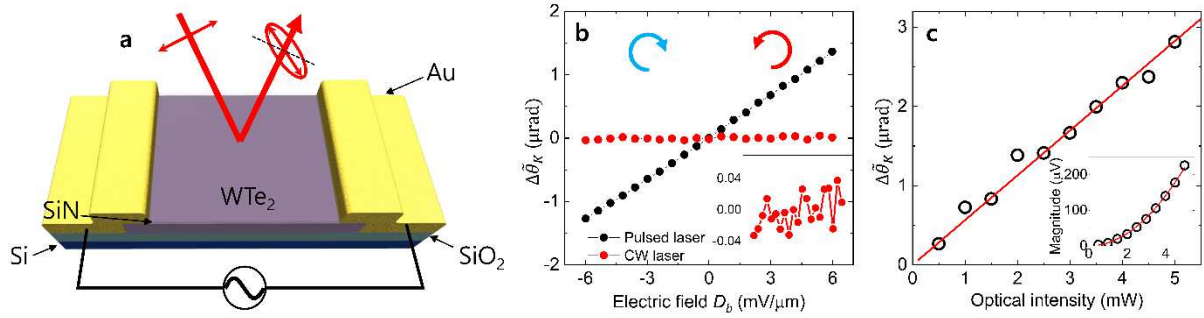
- 396
397 38. Liao, H. B., Xiao, R. F., Wang, H., Wong, K. S. & Wong, G. K.L. Large third-order optical nonlinearity
398 in Au:TiO₂ composite films measured on a femtosecond time scale. *Appl. Phys. Lett.* **72**, 1817-1819
399 (2019).
- 400
401 39. Liu, Y. *et al.* Third-order nonlinear optical response of Au-core CdS-shell composite nanoparticles
402 embedded in BaTiO₃ thin films. *Appl. Phys. B* **76**, 435-439 (2003).
- 403
404 40. Sie, E. J. *et al.* An ultrafast symmetry switch in a Weyl semimetal. *Nature* **565**, 61-66 (2019).
- 405
406
407



408

409 **Fig. 1 | Crystal structure and metallic characteristic of WTe₂ multilayer.** **a**, Top-view of WTe₂
 410 thin film. Red arrow indicates light polarization direction with an angle θ with respect to *a*-
 411 axis (solid line). Dashed line implies mirror plane. **b**, Polarization dependent Raman spectra
 412 along the different crystal directions of WTe₂. **c**, Fourier transform pattern from a transmission
 413 electron microscopy image of WTe₂ crystal showing the *a*- and *b*-axis directions. **d**, Optical
 414 microscope image of the investigated WTe₂ device. Scale bar is 5 μm . **e**, Current-voltage
 415 characteristics of the *a*- and *b*-axis devices at room temperature. **f**, Temperature-dependent
 416 resistivities of the devices showing the metallic behavior of WTe₂ multilayer.

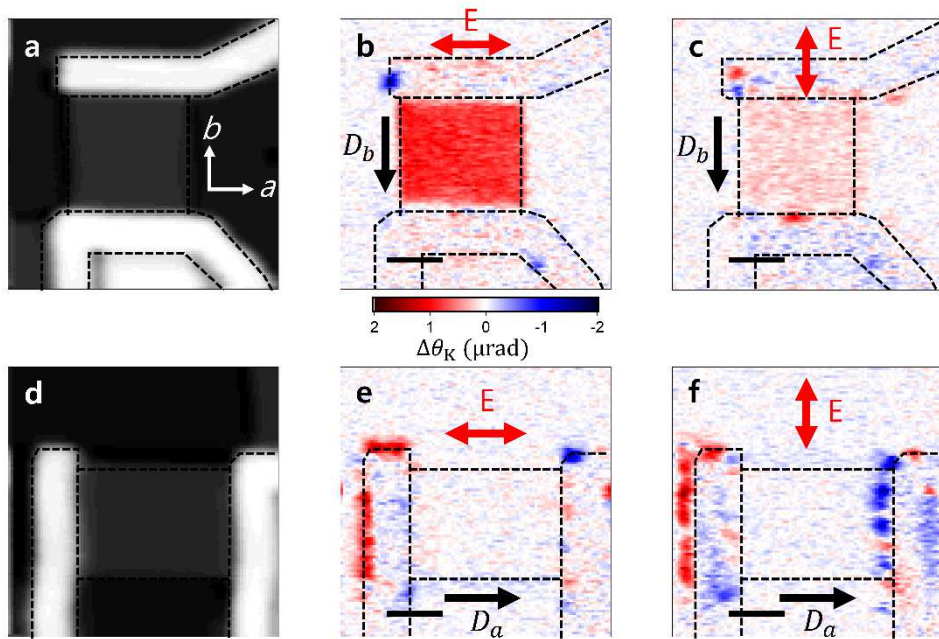
417



418

419 **Fig. 2| Current-induced nonlinear Kerr rotation in WTe₂ multilayer.** **a**, Schematic
 420 illustration of opto-electronic Kerr measurement for WTe₂ device. Red arrows indicate laser
 421 probing beam and its polarization directions. **b**, Kerr rotation as a function of the displacement
 422 field D_b . Kerr rotation is linearly proportional to D_b , and its sign is reversed when the direction
 423 of D_b is opposite. The observed Kerr angle is much lower with continuous wave laser excitation
 424 (red open circles) compared to the case of pulsed laser excitation (black dots). The inset shows
 425 the enlarged graph of the continuous wave laser case. Optical power is the same for each case.
 426 **c**, Kerr rotation as a function of the optical power. The linear dependence on the optical power
 427 implies the optically nonlinear process. The inset shows that the raw signal (ΔI) depends
 428 quadratically on the optical power.

429



430

431 **Fig. 3| Spatial scan of Kerr rotation with different directions of charge current and light**
 432 **polarization. a,d,** Reflectance mapping images of the *b*-axis and *a*-axis devices. Scale bars
 433 indicate 5 μm . **b,c,** Kerr rotation mappings of the *b*-axis device with different directional light
 434 polarization **e,f,** Kerr rotation mappings of the *a*-axis device with the different directions of
 435 light polarization. Black and red arrows indicate the directions of the \vec{D} of charge current and
 436 \vec{E} of input light.

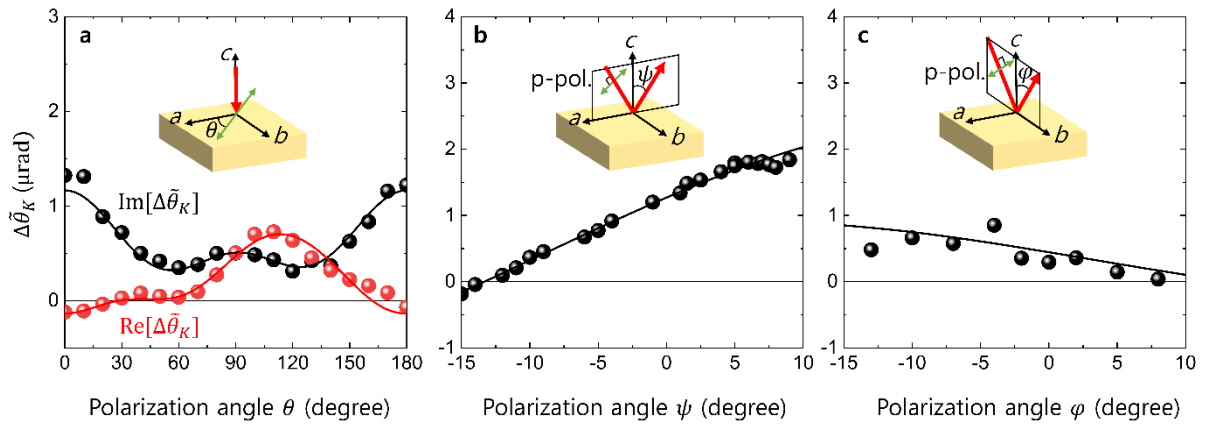
437

438

439

440

441



442

443 **Fig. 4| Kerr rotation with a three-dimensional variation of polarization of light.** a, Kerr
 444 rotation angle results as a function of azimuth angle, θ , at a normal incidence geometry. Black
 445 and red data are imaginary and real part of the Kerr angle, respectively. b,c, Imaginary Kerr
 446 angle results as a function of grazing incidence angle ψ and φ at an oblique incidence plane
 447 of a-c and b-c, respectively, with p-polarization of incident light.

Figures

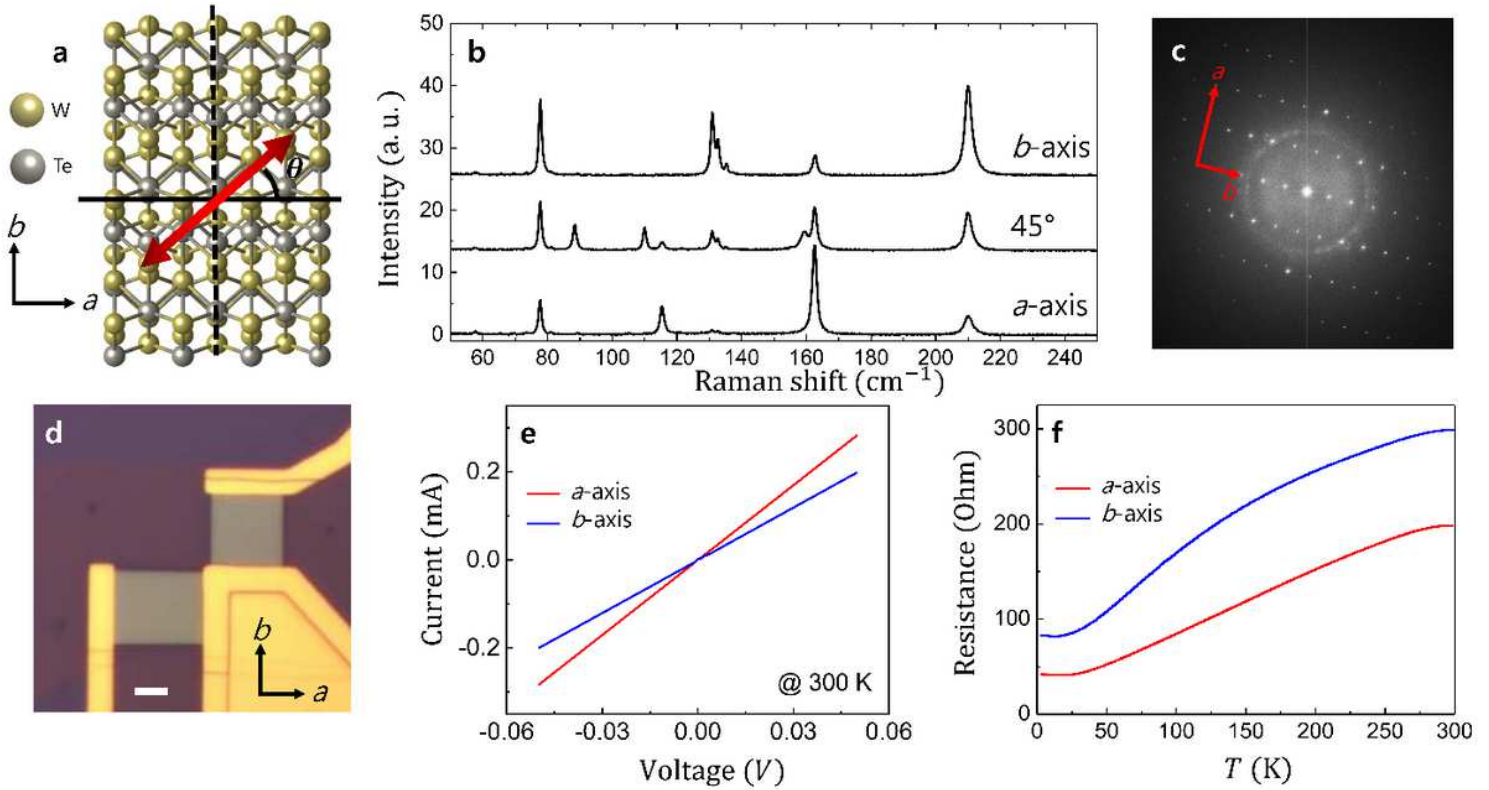


Figure 1

Crystal structure and metallic characteristic of WTe₂ multilayer. a, Top-view of WTe₂ thin film. Red arrow indicates light polarization direction with an angle θ with respect to a-axis (solid line). Dashed line implies mirror plane. b, Polarization dependent Raman spectra along the different crystal directions of WTe₂. c, Fourier transform pattern from a transmission electron microscopy image of WTe₂ crystal showing the a- and b-axis directions. d, Optical microscope image of the investigated WTe₂ device. Scale bar is 5 μm . e, Current-voltage characteristics of the a- and b-axis devices at room temperature. f, Temperature-dependent resistivities of the devices showing the metallic behavior of WTe₂ multilayer.

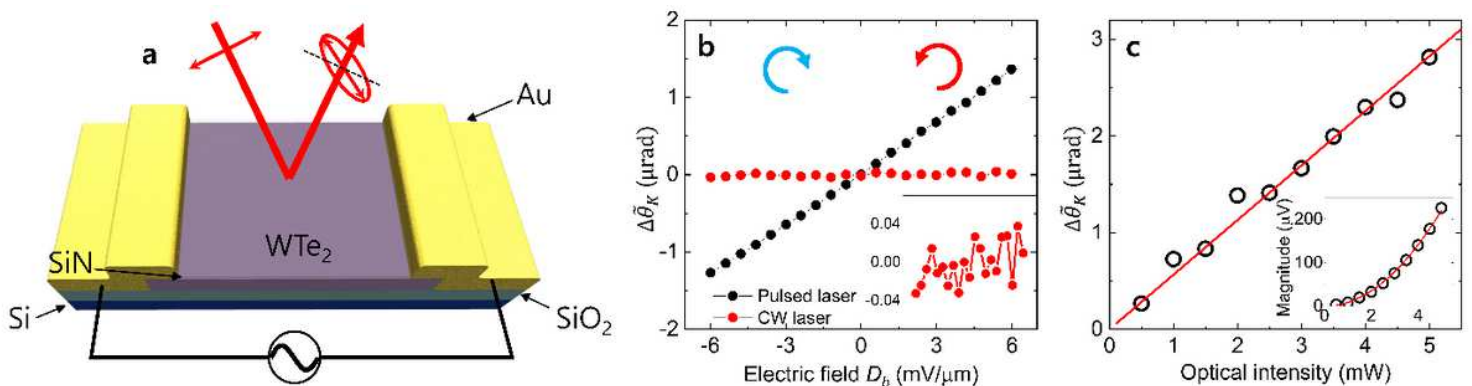


Figure 2

Current-induced nonlinear Kerr rotation in WTe₂ multilayer. a, Schematic illustration of opto-electronic Kerr measurement for WTe₂ device. Red arrows indicate laser probing beam and its polarization directions. b, Kerr rotation as a function of the displacement field D_b . Kerr rotation is linearly proportional to D_b , and its sign is reversed when the direction of D_b is opposite. The observed Kerr angle is much lower with continuous wave laser excitation (red open circles) compared to the case of pulsed laser excitation (black dots). The inset shows the enlarged graph of the continuous wave laser case. Optical power is the same for each case. c, Kerr rotation as a function of the optical power. The linear dependence on the optical power implies the optically nonlinear process. The inset shows that the raw signal (ΔI) depends quadratically on the optical power.

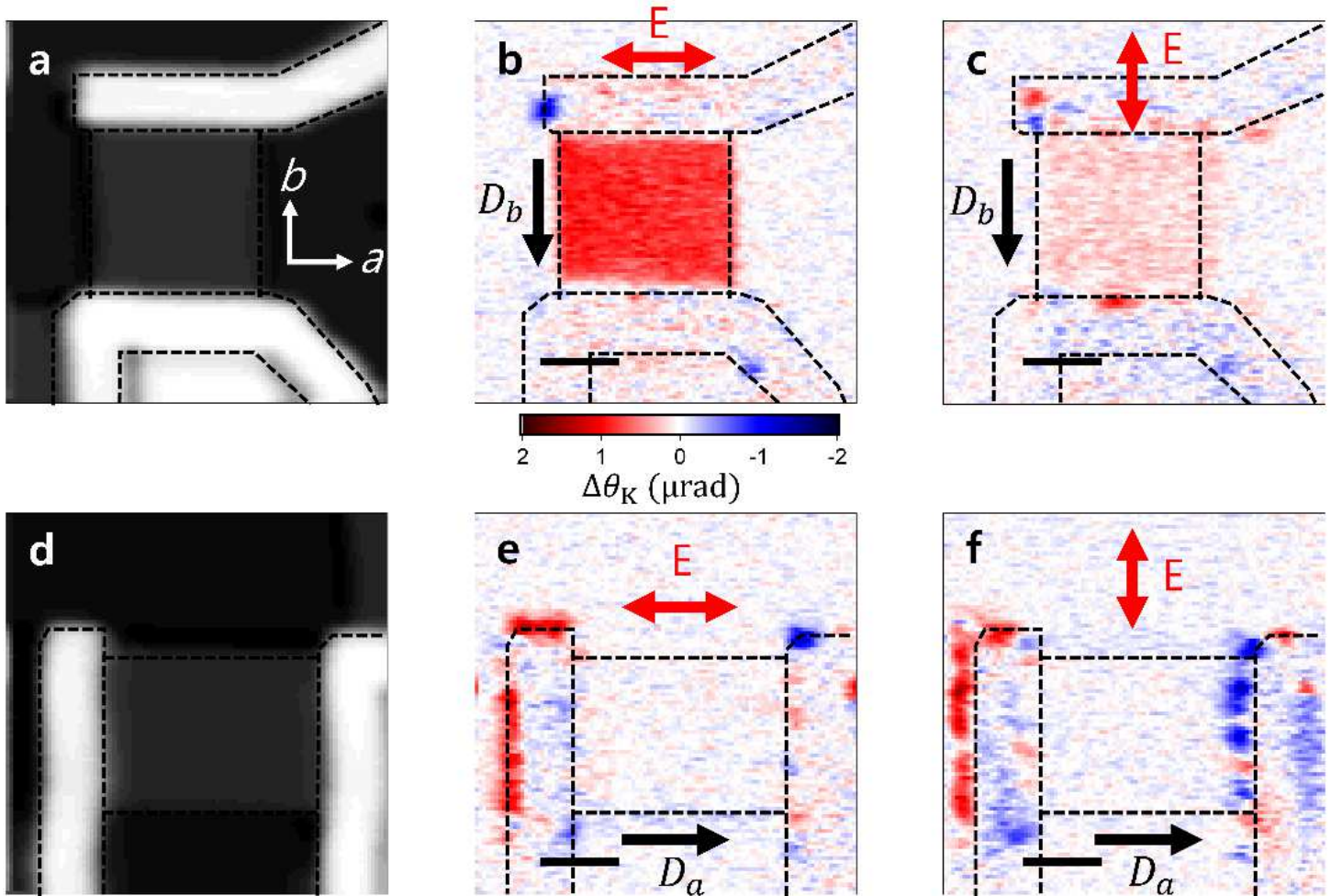


Figure 3

Spatial scan of Kerr rotation with different directions of charge current and light polarization. a,d, Reflectance mapping images of the b-axis and a-axis devices. Scale bars indicate 5 μm . b,c, Kerr rotation mappings of the b-axis device with different directional light polarization e,f, Kerr rotation mappings of the a-axis device with the different directions of light polarization. Please see manuscript .pdf for full caption.

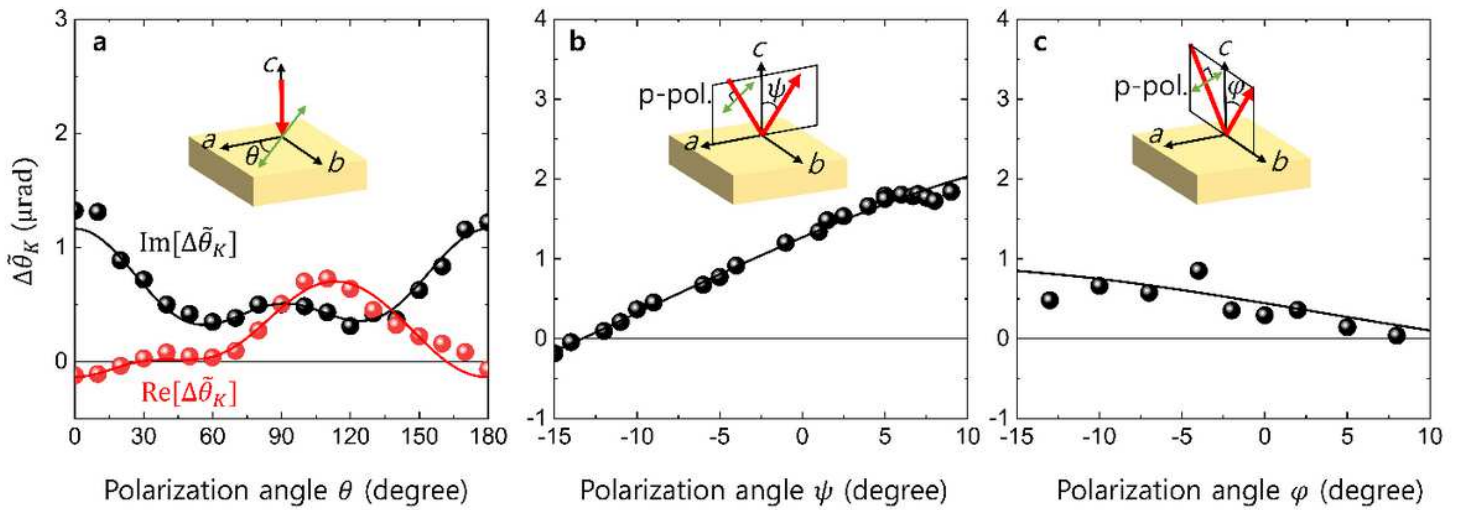


Figure 4

Kerr rotation with a three-dimensional variation of polarization of light. a, Kerr rotation angle results as a function of azimuth angle, θ , at a normal incidence geometry. Black and red data are imaginary and real part of the Kerr angle, respectively. b,c, Imaginary Kerr angle results as a function of grazing incidence angle ψ and φ at an oblique incidence plane of a - c and b - c , respectively, with p-polarization of incident light.

Supplementary Files

This is a list of supplementary files associated with this preprint. Click to download.

- [Slv8.pdf](#)